Proceedings 10th NUMGE 2023
10th European Conference on Numerical Methods in Geotechnical Engineering
Zdravkovic L, Kontoe S, Taborda DMG, Tsiampousi A (eds)

https://doi.org/10.53243/NUMGE2023-10

Numerical modelling of uplifting a surface foundation on clay

S. Mei, Y. Tian, M.J. Cassidy

Department of Infrastructure Engineering, The University of Melbourne, Melbourne, Australia

ABSTRACT: Offshore shallow foundations are required to be retrieved at the end of their life cycle. The required force is much larger than their own submerged weight due to significant suction generated at the invert of the foundation. This paper reports numerical modelling of uplifting a surface foundation whilst employing a hydro-mechanic interface that can capture both mechanic and hydraulic interactions between foundation and soil. The soil behaviour was modelled using the modified Cam-Clay model. After verifying against physical modelling data from centrifuge tests, the numerical results are interpretated in terms of pore pressure distribution at the interface, deformation mechanism and stress path of soils, which enhances the understanding of uplift response of surface footings on clay seabed.

Keywords: uplift, shallow foundation, rate effect, interface, coupled analysis

1 INTRODUCTION

Shallow foundations are used offshore to support platforms, pipelines and manifolds and as anchoring systems (Bye et al., 1995; Bouwmeester et al., 2009; Randolph and Gourvenec, 2010). They are required to be decommissioned at the end of their life cycle (Gourvenec, 2018). The extraction force required often exceeds their own submerged weight, especially when the footings sit on fine-grained soils. The excessed resistance emanates from the negative pore pressure (i.e., suction) generated at the invert of the footings during uplift. Accurately predicting the uplift resistance can provide an appropriate guide for vessel deployment and avoid severe safety consequences.

Previous experimental studies on uplift of shallow foundations (e.g., Chen et al., 2012; Li et al., 2014; Mei et al., 2023) have shown that uplift resistance is rate-dependent. Under rapid uplift, the suction underneath the footing is fully developed and has no time to dissipate. Undrained behaviour with a reverse bearing mechanism is reached with an uplift capacity comparable to compression capacity. Under slow uplift, drained conditions are achieved. The suction is dissipated and the uplift capacity only consists of mobilized footing-soil friction. Between these two extremes, an intermediate rate ends up with partially drained conditions.

Compared to compression, numerical modelling of this rate-dependent uplifting process is far more challenging. Firstly, a coupled analysis of soil and water is required within the effective-stress framework as excess pore pressure is involved. Secondly, appropriate modelling of the interface between the footing and soil is complex but essential. During uplift, negative pore pressure is generated at the foundation invert where a gap may be formed. The fluid flow driven by the suction fills the opening gap. This hydraulic behaviour cannot be described by a simply fully bonded interface (such as the one adopted in Li et al., 2015) or purely mechanical interface models, which is not a problem in compression modelling.

This paper reports numerical modelling of uplifting a surface footing on clay seabed using a hydro-mechanic interface model that can capture both the mechanic behaviour and hydraulic behaviour (Cerfontaine et al, 2015; Peng et al., 2022; Tian et al., 2022). The soil behaviour of the seabed was modelled by the elastoplastic modified Cam-Clay (MCC) model (Roscoe and Burland, 1968). The numerical model was verified against a series of physical geotechnical centrifuge tests reported in Mei et al. (2023). The numerical results are discussed and interpreted to improve the understanding of uplifting problems.

2 NUMERICAL MODEL

The small strain finite-element analysis presented in this paper was carried out using commercial software ABAQUS (Dassault Systèmes, 2016).

2.1 Geometry and materials

An axisymmetric numerical model was established to retrospectively simulate the centrifuge tests of Mei et al. (2023) as shown in Fig. 1. The soil region was set as five times the footing diameter D, which was far enough to eliminate boundary influence. The footing was modelled as a rigid body and had a reference point at the top centre. The footing and the soil were discretised as 4-node elements named CAX4R and CAX4P in the

ABAQUS element library, respectively. The soil behaviour was defined by the MCC model, which uses an associated flow. The MCC parameters are listed in Table 1, which are fit from laboratory test on the same type of kaolin clay used in the centrifuge tests (O'Loughlin, 2022). Among them, the permeability was deduced from the consolidation coefficient obtained from the Rowe cell test at the stress level at depth of $D/6$. The permeability was assumed to be isotropic in the numerical simulation of lightly overconsolidated clay with OCR = 2, as the soil horizontal and vertical permeabilities are reported to be close in the reconstituted NC clay samples in the centrifuge (Vessia et al., 2012).

Table 1. Parameters of the numerical model

Parameter	Value
Soil	
Angle of internal friction, φ'	23°
Void ratio at p'=1 kPa on virgin consolidation line, e_N	3.96
Slope of normal consolidation line, λ	0.435
Slope of swelling line, κ	0.063
Poisson ratio, ν'	0.3
Submerged density, ρ': kg/m^3	260
Permeability, k: m/s	5×10^{-8}
Interface	
Threshold gap size, δ: m	1×10^{-3}
Leak-off coefficient, c: m/(s·kPa)	1×10^{-3}
Tangential permeability, k_x: m/s	5×10^{-8}
Fluid dynamic viscosity, μ: kPa·s	1×10^{-6}

The numerical simulations were conducted in terms of model surface footing with D = 0.06 m in the centrifuge at an acceleration of 40 g in order to make straightforward comparisons. In the numerical analysis, the earth pressure coefficient in the lightly overconsolidated soil is

$$K_0^{oc} = K_0^{nc}\mathrm{OCR}^{\sin\varphi'} = (1-\sin\varphi')\mathrm{OCR}^{\sin\varphi'} \quad (1)$$

where K_0^{nc} is the earth pressure coefficient of normally consolidated soil, φ' is the effective internal friction angle. The OCR is the ratio between the maximum vertical effective stress experienced by the soil σ_{vm}' and the initial vertical effective stress σ_{v0}':

$$\sigma_{vm}' = \sigma_{v0}'\mathrm{OCR} \quad (2)$$

The size of the yield envelope is linked to the maximum mean effective stress p_m' and deviatoric stress q_m:

$$p_c' = \frac{q_m^2}{M^2 p_m'} + p_m' \quad (3)$$

with $M = \frac{6\sin\varphi'}{3-\sin\varphi'}$, $q = sign(\sigma_v' - \sigma_h')\sqrt{2J_2}$.

The initial void ratio of a soil element is given as

$$e_0 = e_N - (\lambda-\kappa)\ln p_c' - \kappa p_0' \quad (4)$$

where e_N is the void ratio at p' = 1 kPa on normally isotropic consolidation line.

The undrained shear strength of overconsolidated soils can be deduced based on the MCC model parameters as below (Potts and Zdravkovic, 1999):

$$s_u = \sigma_{v0}'\left[\mathrm{OCR}g(\theta)\cos\theta\frac{(1+2K_0^{nc})}{6}(1+A^2)\right]\times \left[\frac{2(1+2K_0^{oc})}{(1+2K_0^{nc})\mathrm{OCR}(1+A^2)}\right]^{\kappa/\lambda} \quad (5)$$

where $g(\theta) = \frac{\sin\varphi'}{\cos\theta+(1/\sqrt{3})\sin\theta\sin\varphi'}$

$$A = \frac{\sqrt{3}(1-K_0^{nc})}{g(-30°)(1+2K_0^{nc})}$$

with θ being the Lode's angle (taken as 0 for plain strain strength). To match the s_u profile in the centrifuge tests, the submerged density of soil was reduced from 400 (measured in the centrifuge tests) to 260 kg/m^3. Then, the obtained undrained shear strength profile (in unit of kPa) was $s_u = 0.8 + 52.6z$, where z is the depth in unit of m.

To improve the numerical stability, a thin layer of soil underneath the interface was modelled by the elastic model with E = 3000 kPa and ν' = 0, as recommended in Cerfontaine et al. (2016).

The interface was located between the footing and the soil, and its upper and lower boundaries were tied to the footing and the soil, respectively. The footing, the interface and the underneath soil had consistent element sizes in horizontal direction, as shown in the close-up view of Fig. 1 and Fig. 2. This is helpful for the interface to be functioning well.

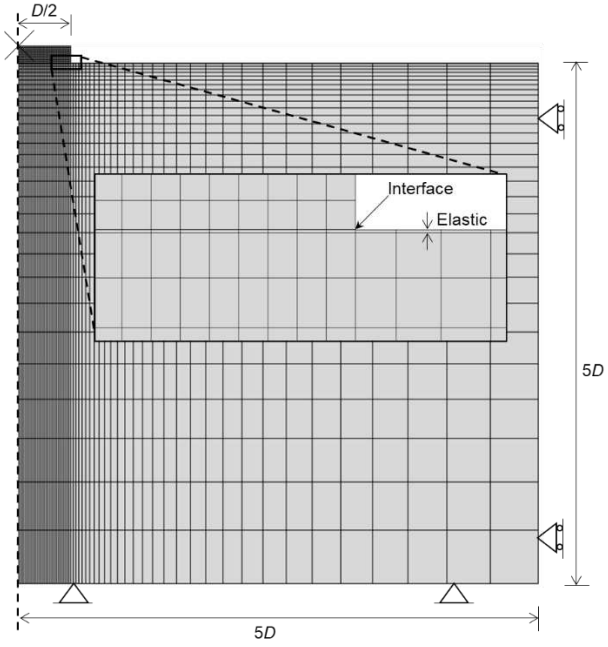

Figure 1. Finite-element mesh

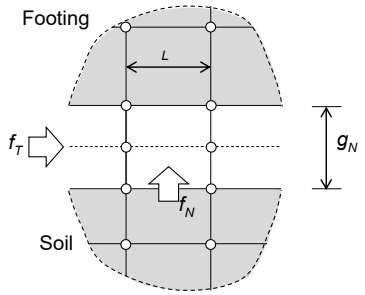

Figure 2. Interface model

2.2 Interface model

An appropriate interface between the foundation invert and the soil is the key to modelling uplifting. The hydro-mechanic interface model applied in this paper was a layer of 6-node elements, labelled as CODAX4P in the ABAQUS element library as illustrated in Fig. 2. The top and bottom four nodes have degree of freedom (DoF) of displacement and pore pressure, while the two middle nodes only have pore pressure DoF.

The fluid flow within an interface element was simplified as normal flow from the soil and tangential flow along the interface (Fig. 2). The normal flow was defined by a 'leak-off model' (Gerke and Genuchten, 1993) as

$$f_N = Lc\Delta p_w \tag{6}$$

where f_N is the normal flow rate, L is the element size, c is the leak-off coefficient, and Δp_w is the differential pressure between the middle and bottom nodes of the interface element (noting the bottom nodes have the same pore pressure as the soil surface).

For tangential flow along the interface, there are two flow modes that can be considered. If the gap is small enough that the gap flow is amid soil particles, the flow can be deemed to obey Darcy's law (termed as Darcy flow here). The tangential flow rate is

$$f_T = \frac{k_x \delta}{\gamma_w} \nabla p \tag{7}$$

where k_x is the tangential permeability (in dimension of L/T), δ is a threshold gap size for Darcy flow, γ_w is the unit weight of water, ∇p is the gradient of pore pressure along the element.

If the gap is large engough that the pure fluid flow is along the interface, the flow can be described by the Navier-Stokes equations. The Poiseuille flow (Schlichting and Kestin, 1961) can be deduced by ignoring the acceleration terms:

$$f_T = \frac{g_N^3}{12\mu} \nabla p \tag{8}$$

where μ is the fluid dynamic viscosity.

Previous studies (e.g., Cerfontaine et al., 2015; Tian et al., 2022; Peng et al., 2022) solely treated the tangential flow as either Poiseuille flow or Darcy flow. A more appropriate approximation of tangential flow is supposed to transition from Darcy flow to Poiseuille flow with an increase in gap opening. When the foundation initially sits on the soil, the gap is closed ($g_N = 0$) and thus the tangential flow is deemed obeying Darcy flow. When the footing moves apart from the soil enough (e.g., the gap size is larger than a threshold gap size ($g_N \geq \delta$)), the tangential flow is assumed to obey Poiseuille flow. Before the gap reaches the threshold ($0 < g_N < \delta$), the flow is in a transition stage and interpolated between Darcy flow and Poiseuille flow:

$$f_T = \left\{\left[1 - \left(\frac{g_N}{\delta}\right)^2\right] \frac{k_x \delta}{\gamma_w} + \left(\frac{g_N}{\delta}\right)^2 \frac{g_N^3}{12\mu}\right\} \nabla p \tag{9}$$

The threshold gap size δ was taken as 1 mm ($1/60D$) in this study, which is shown to be a reasonable magnitude for the transition (see the comparison of physical and numerical results in section 3).

The fluid within the interface elements obeys mass conservation with consideration of normal and tangential flow and the rate of gap opening. The interface papameters are listed in Table 1.

2.3 Boundary conditions and loading

As shown in Fig.1, the bottom of the soil domain was fixed both horizontally and vertically, while the right boundary of the soil was constrained only horizontally. The soil surface, except for along the footing, was set as a zero (excess) pore pressure boundary. The edge of the interface element was exposed to the ambient free water, and thus it was also defined as a drainage boundary, i.e., zero (excess) pore pressure. In the numerical modelling, the initial stress and pore pressure of the numerical model was first self-balanced in a geostatic step. Then, in the subsequent loading step, the reference point of the footing was vertical uplifted at varying uplift rates ranging from 1×10^{-7} to 1×10^{8} mm/s.

3 COMPARISON WITH EXPERIMENT RESULTS

The constitutive model of the soil used in the numerical modelling is a non-viscous model ignoring strain rate effects. To facilitate comparison between the numerical and the experimental results, the experimental results presented below have strain rate effects subtracted (as discussed in Mei et al. (2023)).

Fig. 3(a) shows typical uplift curves under varying uplift rates from the numerical simulation, and Fig. 3(b) illustrates their comparison with the experiment results under three uplift rates, where the horizontal axis is the dimensionless displacement w/D and the vertical axis is the dimensionless uplift resistance F/As_{um}, where A is the foundation plate cross area and s_{um} is the undrained

shear strength at the surface. The uplift velocity is normalized based on $V = vD/c_{op}$, where c_{op} is the operative consolidation coefficient and taken as 0.25 mm^2/s (Mei et al., 2023). The uplift resistance increased with the uplift displacement until reaching a peak, and then dropped to zero. Higher uplift rates result in larger peak resistance and gentler post-peak drop, which is consistent with the experimental observations. The peak resistances on the uplift curves are taken as the uplift capacity for each case. The uplift capacities in the numerical simulation are consistent with those in the experiment, although the uplift stiffness in numerical results is larger. This might be due to elastic deformation of soil within the initial yield surface which exaggerates the stiffness of soils. This paper focuses on the uplift capacity, and the stiffness of the uplift response is not intended to be intensively explored.

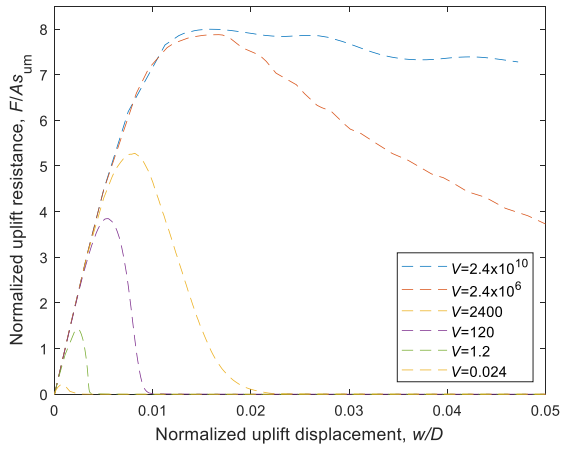

(a)

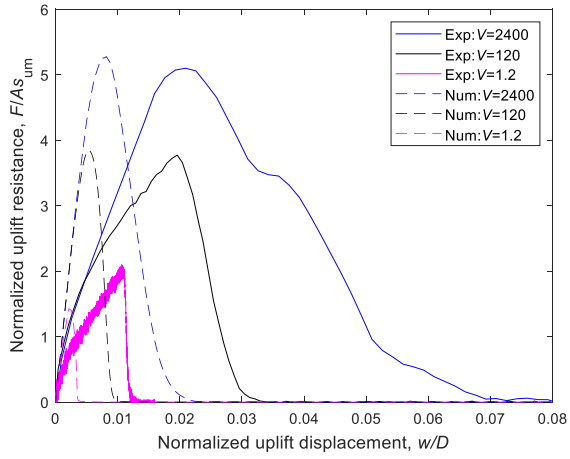

(b)

Figure 3. Uplift curves under various uplift rates: (a) numerical results; (b) comparison with experiment results

As shown in Fig. 4, a backbone curve is established by plotting uplift capacity factors N_{up} (i.e., the dimensionless peak resistance) against dimensionless uplift velocities V. The undrained capacity factor from compression test conducted in Mei et al. (2023) is plotted as a dotted line. When $V > 2.4\times10^{7}$, undrained conditions are achieved, and the uplift capacity is equal to the undrained compression capacity. $V < 2.4\times10^{-3}$ reaches drained conditions where the uplift capacity is near zero. Between these two limits are partially drained conditions.

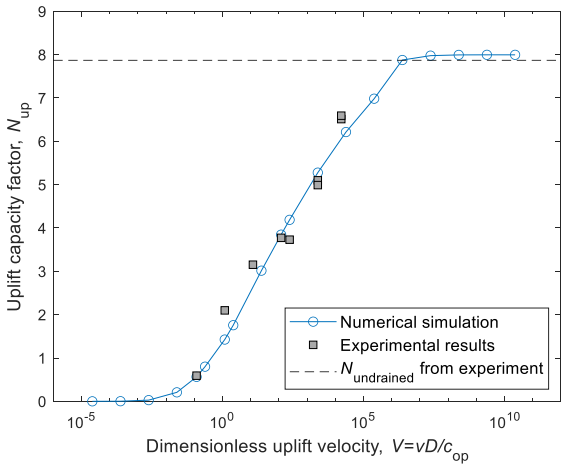

Figure 4. Backbone curve of uplifting

4 INTERPRETATION OF NUMERICAL RESULTS

Numerical modelling provides an effective way to visualize the pore pressure distribution, deformation mechanisms and stress path of the soil during uplift.

Fig.5 illustrates the excess pore pressure distribution along the footing radius under various uplift rates at the peak resistance. The generated excess pore pressure was negative in all cases (except a spike near the edge in some cases, which is believed to be a numerical issue). Higher uplift rate results in larger negative pore pressure generation. For each case, the negative pore pressure was generally larger within the central area than near the edge where some oscillation exists. Integration of the pore pressure with the area underneath the footing is shown to be equal to the uplift resistance. This means that the uplift resistance was completely contributed from negative pore pressure and that the soil particles do not provide 'effective' tension.

Fig. 6 shows the soil displacement vector plot at the peak resistance representing the soil flow mechanism. Under drained conditions, the soil is hardly mobilized. With the increase of uplift velocity, the soil deformation increases. When the undrained conditions are achieved, a reverse bearing mechanism is fully mobilized.

Fig. 7 illustrates the gap opening size g_N along the footing radius at the peak normalized by the corresponding upward displacement w under different rate uplifts. At the rapidest uplift rate ($V = 2.4\times10^{10}$), the gap hardly opened except near the interface edge where the drainage boundary existed. With a decrease in uplift velocity, the gap opening increased with larger gap near the edge than at the centre. This causes more rapid decrease in the uplift resistance during the post-peak period (Fig. 3). At

a low uplift rate (i.e., $V = 0.0024$), the gap opening was almost equal to the upward displacement.

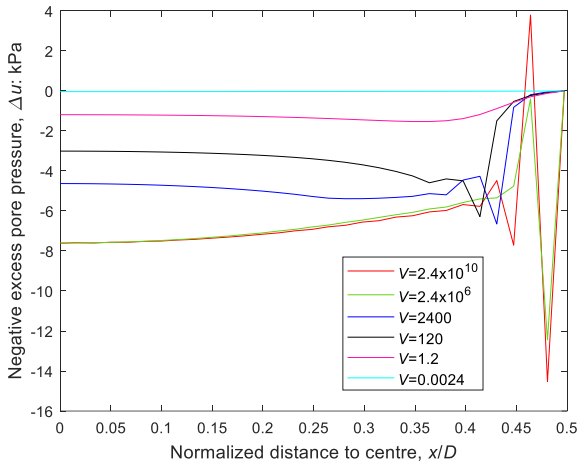

Figure 5. Excess pore pressure distribution at the interface

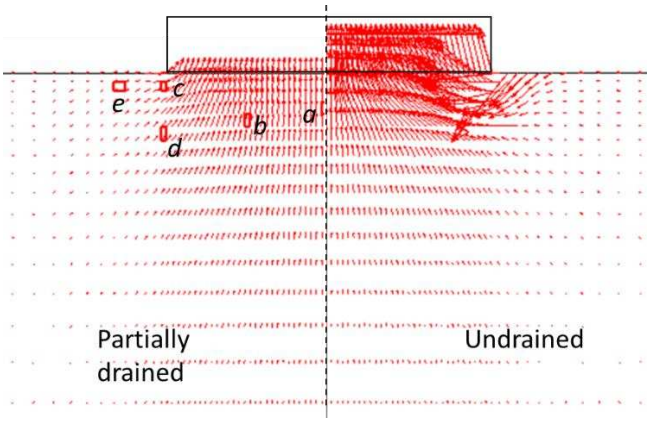

(a) *(b)*

Fig. 6. Deformation mechanism under partially drained (a) and undrained (b) conditions

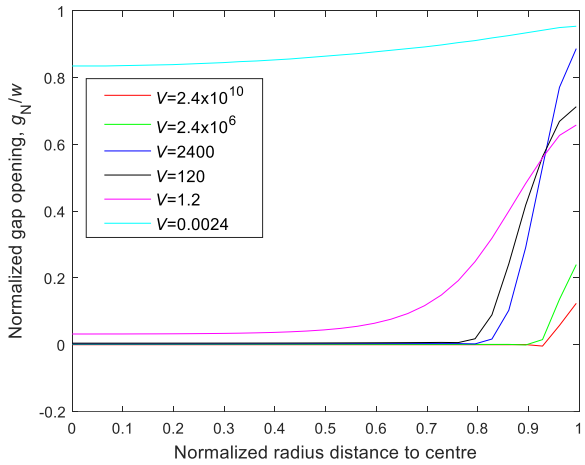

Fig. 7. Gap opening at the interface

Fig. 8. illustrates the stress path of typical soil elements labelled as *a*~*e* in Fig. 6(a) under drained, partially drained and undrained conditions in p'-q plane. The soil was initially under $K0$ state with OCR = 2. Thus, the initial stress on the $K0$ state line ($K0$-SL) was inside the initial yield surface and on the 'dry side' of the MCC model. Under undrained conditions, the soil stress changed with effective mean stress p' constant within the initial yield surface. When it started yielding, the stress moved toward the critical state line (CSL) with the yield surface shrinking until reaching critical state.

Under partially drained conditions, only some soil elements (e.g., *a* and *b*) were yielded, while other soil elements (e.g., *c*, *d* and *e*) was in elastic state within the initial yield surface.

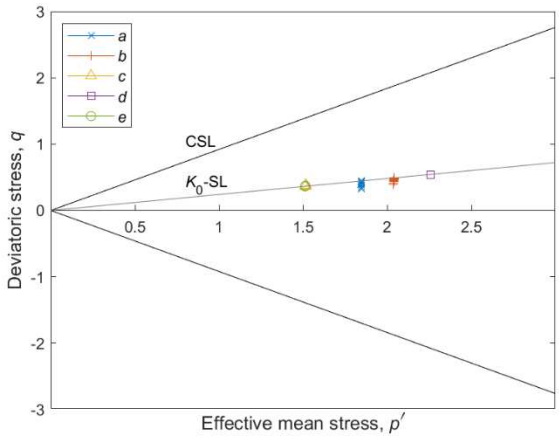

(a)

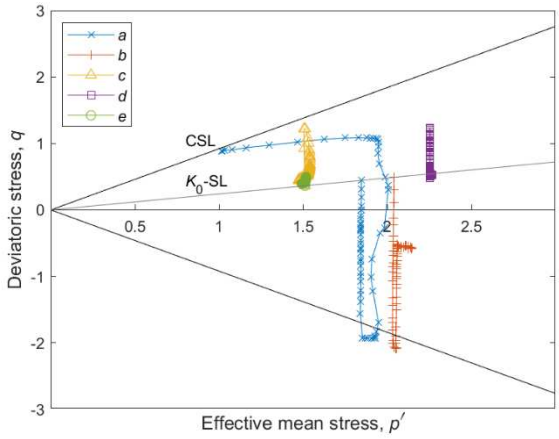

(b)

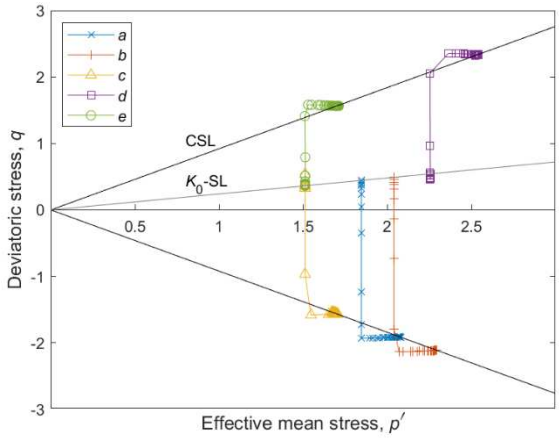

(c)

Fig. 8. Stress path of soil elements under drained (a), partially drained (b) and undrained (c) conditions

Under drained conditions, the stress had negligible changes as the soil was hardly mobilized. In Li et al. (2015) where the foundation and soil were bonded without using a hydro-mechanic interface, even under very low uplift rate the soil experienced unloading and provided unrealistic effective tension force, which resulted in relatively large uplift resistance. This illustrates the effectiveness of employing hydro-mechanic interface when modelling uplifting problems.

5 CONCLUSIONS

Numerical modelling of uplifting a surface footing under varying uplift rates was achieved by utilizing a hydro-mechanic interface. The numerical model was verified against the centrifuge test results. Uplift curves and uplift capacities are consistent between the numerical and experimental results. The mobilized capacity ranges from undrained capacity under rapid uplift to zero under slow uplift. The numerical results were interpreted to uncover the mechanism of uplift. During uplift, the uplift resistance is found to derive from negative pore pressure (suction) generated underneath the foundation plate without any effective mechanical tension force. Rapid uplift results in mobilization of the reverse undrained bearing mechanism without separation between soil and foundations and soil elements experienced yielding with no volumetric strain. Under an intermediate rate soil was partly mobilized and the gap at the interface gradually opened from the interface side to the central. Under slow uplift, the soil was hardly mobilized as little suction was generated with gap nearly fully opened.

6 ACKNOWLEDGEMENTS

This research was undertaken with support from Australian Research Council Discovery Projects (DP190103315), Future Fellowship (FT200100457).

7 REFERENCES

Bouwmeester, D., Peuchen, J., Van der Wal, T., Sarata, B., Willemse, C. A., VanBaars, S., Peelen, R. 2009. Prediction of breakout force for deep water seafloor objects. *In Proceedings of the Offshore Technology Conference*, Houston, Tex. OTC 19925.

Bye, A., Erbrich, C., Rognlien, B., Tjelta, T.I. 1995. Geotechnical design of bucket foundations. *In Proceedings of the Annual Offshore Technology Conference*, Houston, Texas, Paper OTC 7793.

Cerfontaine, B., Dieudonné, A. C., Radu, J. P., Collin, F., Charlier, R. 2015. 3D zero-thickness coupled interface finite element: Formulation and application. *Computers and Geotechnics*, 69, 124-140.

Cerfontaine, B., Collin, F., Charlier, R. 2016. Numerical modelling of transient cyclic vertical loading of suction caissons in sand. *Géotechnique*, 66(2), 121-136.

Chen, R., Gaudin, C., Cassidy, M.J. 2012. Investigation of the vertical uplift capacity of deep water mudmats in clay. *Canadian Geotechnical Journal*, 49(7), 853-865.

Dassault Systèmes. 2016. *Abaqus Analysis Users' Manual*. Simulia Corp, Providence, RI, USA.

Gerke, H. H., & Van Genuchten, M. T. 1993. A dual ‐ porosity model for simulating the preferential movement of water and solutes in structured porous media. *Water resources research*, 29(2), 305-319.

Gourvenec, S. 2018. Shaping the offshore decommissioning agenda and next-generation design of offshore infrastructure. *Proceedings of the Institution of Civil Engineers-Smart Infrastructure and Construction*, 171(2), 54-66.

Li, X., Gaudin, C., Tian, Y., Cassidy, M.J. 2014. Effect of perforations on uplift capacity of skirted foundations on clay. *Canadian Geotechnical Journal*, 51(3), 322-331.

Li, X., Tian, Y., Gaudin, C., Cassidy, M.J. 2015. Comparative study of the compression and uplift of shallow foundations. *Computers and Geotechnics*, 69, 38-45.

Mei, S., Tian, Y., Cassidy, M.J., O'Loughlin, C. 2023. Experimental investigation of rate effects on the uplift behaviour of shallow foundations. To be submitted.

O'Loughlin, C. 2022. *Private communication*.

Peng, M., Tian, Y., Gaudin, C., Zhang, L., Sheng, D. 2022. Application of a coupled hydro-mechanical interface model in simulating uplifting problems. *International Journal for Numerical and Analytical Methods in Geomechanics*, 46(17), 3256-3280.

Potts, D.M., Zdravkovic, L. 1999. *Finite element analysis in geotechnical engineering – theory*. London, UK: Thomas Tel-ford.

Randolph, M.F., Gourvenec, S.M. 2010. *Offshore Geotechnical Engineering*. Taylor & Francis, London, ISBN: 978-0-415-47744-4.

Roscoe, K.H., Burland, J. 1968. On the generalized stress-strain behaviour of wet clay. *Engineering Plasticity*. Cambridge, UK: Cambridge University Press. p. 535–609.

Schlichting, H., Kestin, J. 1961. *Boundary layer theory* (Vol. 121). New York: McGraw-Hill.

Tian, Y., Ren, J., Zhou, T., Peng, M., Cassidy, M.J. 2022. Coupled hydro-mechanical interfaces to enable uplift modelling in offshore engineering. *Ocean Engineering*, 245, 110570.

Vessia, G., Casini, F. & Springman, S. M. (2012). Discussion on ‘Estimating hydraulic conductivity from piezocone soundings. *Géotechnique*, 62, No. 10, 955–956.